AWARD NUMBER: W81XWH-11-1-0103

TITLE: **NESTED NANOTHERAPEUTICS FOR DRUG SYNERGY ENHANCEMENT IN BREAST** CANCER THERAPY

PRINCIPAL INVESTIGATOR: **ELVIN BLANCO, PHD**

CONTRACTING ORGANIZATION: **METHODIST HOSPITAL RESEARCH INSTITUTE**

HOUSTON, TX 77030

REPORT DATE: **SEPTEMBER 2014**

TYPE OF REPORT: **Final Summary**

PREPARED FOR: **U.S. Army Medical Research and Materiel Command**
Fort Detrick, Maryland 21702-5012

REPORT DOCUMENTATION PAGE

Form Approved
OMB No. 0704-0188

1. REPORT DATE	2. REPORT TYPE	3. DATES COVERED
Sept 2014	Final Summary	01 Jan 2011 – 30 Jun 2014

4. TITLE AND SUBTITLE
Nested Nanotherapeutics for Drug Synergy Enhancement in Breast Cancer Therapy

5a. CONTRACT NUMBER

5b. GRANT NUMBER
W81XWH-11-1-0103

5c. PROGRAM ELEMENT NUMBER

6. AUTHOR(S)
Elvin Blanco, PhD

E-Mail:eblanco@HoustonMethodist.org

5d. PROJECT NUMBER

5e. TASK NUMBER

5f. WORK UNIT NUMBER

7. PERFORMING ORGANIZATION NAME(S) AND ADDRESS(ES)
Methodist Hospital Research Institute

Houston, TX 77030

8. PERFORMING ORGANIZATION REPORT NUMBER

9. SPONSORING / MONITORING AGENCY NAME(S) AND ADDRESS(ES)
U.S. Army Medical Research and Materiel Command
Fort Detrick, Maryland 21702-5012

10. SPONSOR/MONITOR'S ACRONYM(S)

11. SPONSOR/MONITOR'S REPORT NUMBER(S)

12. DISTRIBUTION / AVAILABILITY STATEMENT
Approved for Public Release; Distribution Unlimited

13. SUPPLEMENTARY NOTES

14. ABSTRACT
Time-staggered and sequential combination chemotherapy strategies show immense potential in controlled cell culture systems, but fail to successfully translate to the clinic due to different routes of administration and disparate formulation parameters that preclude a specific order of drug presentation. We have rationally designed a novel nanoparticle construct capable of releasing drugs in a time- and sequence-dependent manner specifically within tumors. The platform consists of drug-containing PLGA polymer nanoparticles stably fashioned with an outer shell composed of drug complexed with cationic cyclodextrin. Morphological examination of nanoparticles, measuring 150 nm in diameter, highlighted compartmentalization of model drugs, rhodamine and bodipy, within the core and shell, respectively. Sequential release was observed *in vitro*, kinetics that were also observed in breast cancer cells following internalization. Sequential-based release was corroborated via confocal microscopy in a murine model of breast cancer following intravenous administration. Incorporation of rapamycin in the outer shell and paclitaxel in the inner core demonstrated sequential release kinetics, significant cell-killing potential, and a substantial reduction of tumor growth in murine models of breast cancer, highlighting the synergistic mechanism of action arising from sequential delivery.

15. SUBJECT TERMS
PI3k/Akt/mTOR pathway, breast cancer, cancer nanomedicine, paclitaxel, rapamycin, drug delivery

16. SECURITY CLASSIFICATION OF:			17. LIMITATION OF ABSTRACT	18. NUMBER OF PAGES	19a. NAME OF RESPONSIBLE PERSON
a. REPORT	b. ABSTRACT	c. THIS PAGE			USAMRMC
U	U	U	UU	25	19b. TELEPHONE NUMBER *(include area code)*

Table of Contents

Introduction

Breast cancer incidence has risen slightly over the last quarter of a century and now makes up one third of new cancer cases in females (1). Combination chemotherapy represents a mainstay treatment modality essential for improvement of survival rates in breast cancer. However, despite numerous regimens employed clinically, patient responses following polychemotherapy remain dismal (2, 3). The chemotherapeutic landscape in breast cancer has evolved considerably in the last few decades, transitioning from the age of anthracyclines (e.g. doxorubicin) to that of taxanes (e.g. paclitaxel), and more recently, to that of repositioned, molecularly-targeted agents (e.g. trastuzumab) (4). Recent molecular insights into underlying signaling pathways and networks suggest that drug synergy in combination chemotherapy may be significantly enhanced if the order of administration, scheduling, and dose duration are given proper consideration (5-7). Findings by several groups have highlighted the therapeutic potential of targeting the phosphatidylinositol 3-kinase (PI3K)/Akt/mammalian target of rapamycin (mTOR) PI3k/Akt/mTOR pathway with agents targeting either PI3k, Akt, or mTOR. (8-10) Rapamycin (RAP), an inhibitor of mTOR, has been shown to have substantial anticancer effects, especially when combined with traditional chemotherapeutics such as cisplatin or paclitaxel (PTX) (7, 11). By delivering agents in a time- and sequence-dependent manner, it may be possible to rewire apoptotic pathways, with one drug chemosensitizing cancer cells to a second drug (12). Strategies where agents are delivered sequentially may also serve to inhibit feedback loops and survival mechanisms inherent to complex signaling cascades by targeting multiple components along the same pathway (13).

While specific combinations of drugs delivered in a time-staggered fashion have been shown to synergistically enhance cell killing preclinically in cell culture systems, this strategy does not translate successfully to the clinic. Pharmacokinetic limitations of conventional drug formulations, including short circulation half-lives and heightened volumes of distribution (14, 15), result in non-specific accumulation of drugs in healthy tissues and insufficient bioavailability in tumors. Moreover, different routes of administration, as well as distinct excipients associated with individual formulations of conventional drugs, result in disparate pharmacokinetic parameters that preclude adherence to strict time constraints specifically in tumors (16), thereby negating therapeutic crosstalk between synergistic agents.

Nanoparticle preparations of traditional chemotherapeutics have substantially improved the pharmacokinetic limitations of agents such as doxorubicin(17) and paclitaxel (18). Encapsulating drugs in nanoscale carriers aids in evasion of sequestration by the reticuloendothelial system (RES), with ensuing increased circulation times resulting in improved nanoparticle accumulation in tumors through the enhanced permeability and retention (EPR) effect (19-21). Past research efforts have focused on the co-encapsulation of drugs within nanoparticles in attempts to enhance synergistic cell killing (22, 23). However, the focus has remained largely on amassing two or more drugs in the tumor with minimal regard for inter-drug synergistic effects, save for a few notable examples (24, 25). Once at the tumor site, release from nanoparticles is dictated by diffusivity parameters and hydrophobicities of drugs, with little to no control over order of drug presentation. As a result, innovative nanoparticles and delivery vectors have emerged with time-staggered drug release kinetics (26-28), highlighting the importance of incorporating time and sequential delivery design parameters into the nanoplatform to ensure maximum synergistic efficacy.

The main objective of the work involved the design and development of a novel nanoparticle platform capable of releasing synergistic agents in a time- and sequence-dependent manner, site-specifically in tumors (Fig. 1). The nanoconstruct, called nested nanoparticles (NNP), consists of a drug-containing polymeric core, composed of poly(lactic-co-glycolic) acid (PLGA), surrounded by an outer shell composed of drug complexed to cationic cyclodextrin (QAβ-CD). PLGA was chosen as the material of the core-forming nanoparticle due to its ability to encapsulate hydrophobic agents (29, 30). Cyclodextrins (CDs) are cyclic

oligosaccharides in the form of truncated cones, and were chosen as the shell forming material because of their ability to form inclusion complexes with hydrophobic drugs, effectively increasing their water solubility (31-33). The nanoplatform comprises a system with independent dual-release kinetics due to the combination of two stand-alone delivery vectors within a single nanoconstruct. Thus, the system represents a departure from current nanoformulations that simply co-encapsulate multiple drugs within a core and are dependent on innate diffusivity parameters for drug presentation. Sequential release of drug from the outer shell followed by release of drug from the nanoparticle core, site-specifically in tumors, stands to significantly impact synergy enhancement in chemotherapy, providing an avenue for successful translation of preclinical time-staggered strategies.

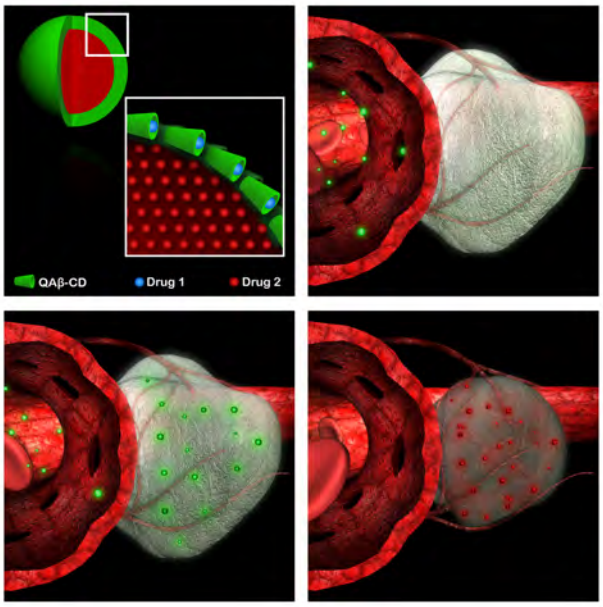

Figure 1. Nested nanoparticles designed for time and sequential release of synergistic therapeutics site-specifically in tumors. The proposed platform consists of drug-containing PLGA nanoparticles with an outer shell composed of drug complexed with cyclodextrin (QAβ-CD). Following intravenous administration, nanoparticles are hypothesized to accumulate in tumors through the enhanced permeability and retention (EPR) effect. Once at the site, drug in the outer shell is released during the early timepoints, chemosensitizing cancer cells to a second drug released at later timepoints from the nanoparticle core, resulting in synergistic enhancement of tumor cell killing.

Throughout the initial part of the sponsored research, nanoparticles were fabricated, and an outer coating based on cyclodextrin complexation technology was formulated. Studies then focused on the optimization of the platform with regards to size, monodispersity, and drug loading. Work was also devoted to the verification of the nested architecture, its stability, as well as accurate control and demonstration of sequence- and time-specific release kinetics. The work in the latter portion of the proposal involved the *in vitro* and *in vivo* efficacy examination of the platform in relevant models of triple negative breast cancer with drugs that work synergistically in a time and sequential fashion. Work towards successful completion of the proposed aims has resulted in the development of a truly innovative nanoparticle platform for synergistic enhancement in breast cancer.

Body

In order to successfully develop the nested nanoplatform, the following aims were proposed:

Aim 1) *Fabrication and characterization of nested nanoparticles containing a drug-loaded core and drug-releasing shell*
Aim 2) In vitro *and* in vivo *efficacy examination of the nested nanoparticle platform in breast cancer cells*

Initial work was devoted to identifying the most suitable core-forming material, as well as developing fabrication methods to ensure small particle size, monodispersity, and favorable drug loading and release. Concomitantly, work towards the development of the outer shell of the nested nanoparticle was conducted, with progress culminating in the development of the

nested nanoparticle. The following sections describe the progress that has been made in pursuit of each task associated with Aim 1.

Fabrication of drug-containing core nanoparticle

The ideal characteristics of the core included the following: 1) high loading of drug within the core; 2) nanoscale size; and 3) slow and sustained release of drug over time ($t_{½}$ of release > 36 h). The polymer chosen for the core-forming polymer was poly(lactic-co-glycolic acid) (PLGA), given its biocompatibility, biodegradability, and FDA approval for a variety of biomedical applications, including drug delivery (34). PLGA particles were fabricated using a previously published single emulsion procedure (35). Briefly, PLGA was dissolved in CH_2Cl_2. The solution was then added to a 1% poly(vinyl alcohol) (PVA) solution under sonication. Following solvent evaporation, the nanoparticles were washed to remove excess PVA and collected via centrifugation. The resulting PLGA particles were characterized for size via light and scanning electron microscopy (SEM). For verification of drug loading, the fluorescent dye rhodamine B was encapsulated (Figure 2A), and the particles examined via fluorescence microscopy. Figure 2 demonstrates the size and loading properties of PLGA particles. As can be observed in the microscopy image comprising Figure 2B, resulting PLGA particles were spherical in shape, albeit very polydisperse in diameter, as verified via scanning electron microscopy (SEM) (Figure 2C). The size of the PLGA particles, as determined by scanning electron microscopy yielded a size range of 4-7 μm in diameter. Particles were found to efficiently load rhodamine B within the core of the particles, as demonstrated qualitatively in the fluorescence microscopy image depicted in Figure 2D. These findings serve to highlight the morphology of the particles, as well as their ability to load agents within the core.

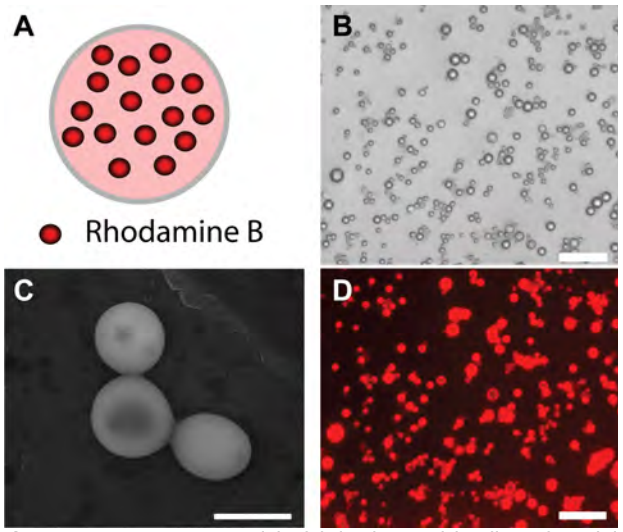

Figure 2. PLGA nanoparticle fabrication and loading of model agent rhodamine B. a. Schematic of PLGA particle containing rhodamine B. b. Phase contrast microscopy image of PLGA particles. The scale bar represents 20 μm. c. SEM image of PLGA particles. The scale bar represents 5 μm. d. Fluorescence microscopy image of rhodamine-containing PLGA particles (red). The scale bar represents 20 μm.

Comprehensive characterization of the particles included examination of the surface charge of the particles as determined by zeta potential analysis. Results demonstrate that the outer surface of the PLGA particles was negative, yielding a value of -29.6 ± 0.34 mV (Figure 3A). This finding was of monumental significance, as it opened a potential avenue for development of an outer drug-containing shell on the PLGA particles via electrostatic interactions. To demonstrate the feasibility of this approach, rhodamine B, a positively charged fluorophore, was once again employed, with the exception that it was added to particles after their formation (Figure 3B). As can be seen in the fluorescence microscopy image comprising Figure 3C, the positively charged rhodamine B was electrostatically grafted to the outer surface of PLGA. This finding was corroborated by confocal microscopy, using a technique involving imaging of sections (i.e. slices) through PLGA particles (Figure 3D). Rhodamine B is localized outside of the particles and not in the core, thus highlighting the ability to electrostatically conjugate a positively charged outer shell to the PLGA particles.

In attempts to generate smaller particles in the nanoscale size range, sonication time, sonication power, and the % of PVA were manipulated. Changes included increasing the sonication time from 1 min to 5 min, increasing the power from 10,000 RPM to 24,000 RPM, and increasing the % of PVA from 1% to 5%. Figure 4 summarizes the findings concerning PLGA particles following fabrication optimization. As can be observed in the SEM images comprising Figures 4A-C, the PLGA particles were again spherical in morphology, but more monodisperse in size, with an average diameter of 300 nm (Figure 4D).

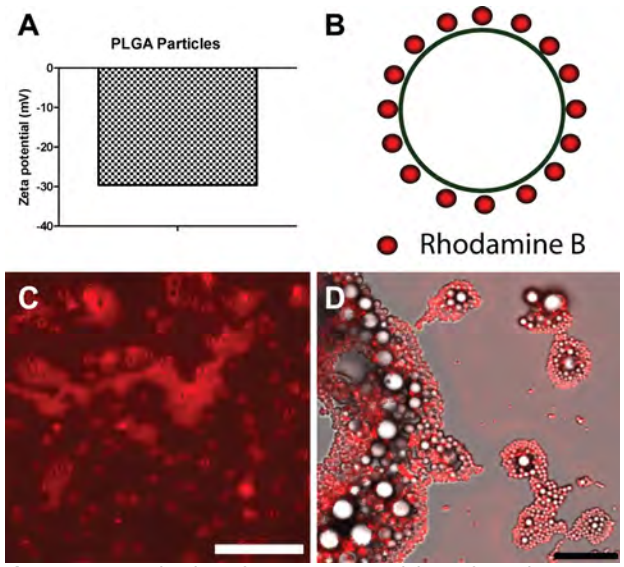

Figure 3. Examination of PLGA nanoparticle surface charge. a. Outer surface charge as determined quantitatively via zeta potential analysis. b. Schematic illustration of PLGA particles with rhodamine B dye bound on the outer surface. c. Fluorescence microscopy image of rhodamine-coated PLGA particles. The scale bar represents 10 μm. d. Confocal microscopy image of PLGA particles with rhodamine on the outer surface. The scale bar represents 100 μm.

While the above findings demonstrate the ability to load drug within spherical PLGA particles, and to graft, electrostatically, an outer, positively charged shell, the size of the particles proved rather large for intravenous applications, warranting modifications to the fabrication protocol to produce smaller, more homogeneous particles. Thus, our goal was to make the entire nanoparticle system smaller in size than its previous incarnation. At the culmination of year 1, the nested nanoparticle measured an average of 488 nm after assembly of its constituent components. While typically employed in *in vivo* drug delivery applications, nanoparticles of this size are less efficacious than smaller nanoparticles, due in large part to increased sequestration by the (RES) and because of reduced tumor penetration (36). This size proved far too large for intravenous drug delivery, and we explored ways to modify the fabrication procedure from year 1 to reduce the overall size of the nanoparticles. To accomplish this, we transitioned from the use of a tissue homogenizer to a probe sonicator, which provided a much greater agitation force in solution, now known to reduce particle size. Briefly, PLGA was dissolved in CH_2Cl_2 and the solution was added to 10% poly(vinyl alcohol) (PVA) under sonication. The resulting nanoparticles were then added to a solution of 5% PVA and left stirring overnight for evaporation of the organic solvent. Following solvent evaporation, the nanoparticles were washed to remove excess PVA and collected via centrifugation.

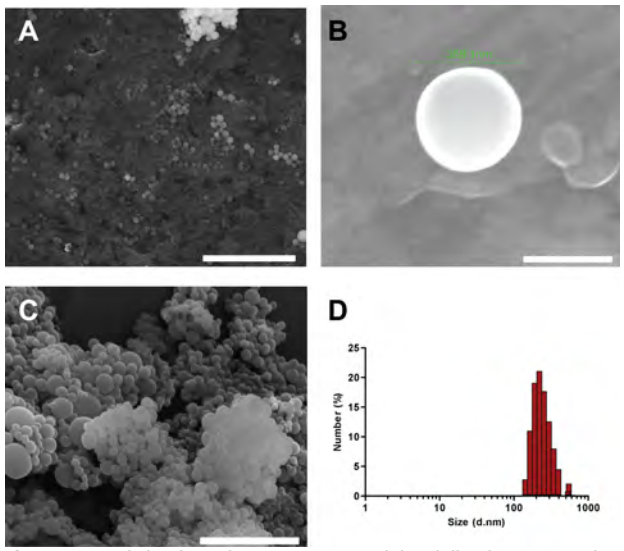

Figure 4. Fabrication of PLGA nanoparticles following protocol optimization. a-c. SEM micrographs of PLGA particles. The scale bar represent 5 μm, 300 nm, and 4 μm, respectively. d. Dynamic light scattering (DLS) results of PLGA particles.

Development of drug-containing outer shell

The nested nanoparticle platform is designed to have an outer drug-containing shell, which is to be released prior to the contents of the core. Having established the core-forming nanoparticle, development of the drug-containing outer shell was undertaken. Ideal properties of the outer shell include the following: 1) high loading/concentration of drug; 2) maintenance of small overall nanoparticle size; 3) stable grafting onto particles; and 4) fast release of drug over time ($t_{½}$ of release < 18 h). In light of the potential avenue for functionalizing PLGA particles with an outer shell via electrostatic interactions, a positively charged cyclodextrin (CD) was chosen as the constituent component of the outermost shell of the nested nanoparticle. Cyclodextrins are cyclic oligosaccharides in the form of truncated cones consisting of a hydrophobic core and a hydrophilic outer surface, widely used in the pharmaceutical industry (37). The unique chemistry of cyclodextrins allows for solubilization of numerous water-insoluble drugs, and has been utilized clinically over the last few decades (38). Hence, quaternary ammonium cyclodextrin (QAβ-CD) was explored as a potential shell-forming material, given its ability to solubilize paclitaxel, as well as its positive charge, allowing it to graft electrostatically to the negatively charged outer surface of the PLGA particle. In order to examine the feasibility and efficiency for this electrostatic interaction, QAβ-CD was complexed with a green fluorescent fluorophore, bodipy, using a previously established procedure (39). Briefly, cyclodextrin was dissolved in water, and an excess of bodipy was added to the solution and stirred overnight. Following overnight stirring, the solution was collected and filtered using a 0.45 μm nylon filter.

Examination of adhesion force between QAβ-CD and PLGA

A firm and stable adhesion between the shell-forming material, QAβ-CD, and PLGA nanoparticles proved critical towards the overall success of the proposed platform. It was initially hypothesized that electrostatic interactions between the positively charged quaternary ammonium associated with QAβ-CD and the negatively charged PLGA surface would provide a stable core-shell construct. Therefore, nanoindentation experiments using atomic force microscopy (AFM) were performed to measure the adhesive force between the component parts, employing tips modified with QAβ-CD and a surface covered with PLGA nanoparticles (Fig. 5a). As can be observed in the AFM image comprising Fig. 5b, the substrate was comprehensively overlaid with PLGA nanoparticles. Fig. 5c comprises force-distance curves achieved from pull-off experiments between the QAβ-CD-coated AFM tip and PLGA nanoparticles and control substrates. Following indentation of the PLGA and control surfaces to a desired force value, retraction of the cantilever was examined. The strong adhesion between the tip and the PLGA nanoparticles caused the

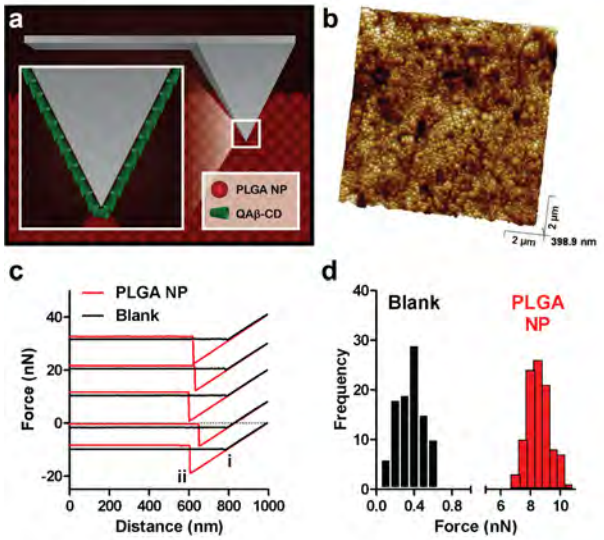

Figure 5. AFM examination of adhesive force between QAβ-CD and PLGA. a. Schematic illustrating the QAβ-CD-functionalized AFM tip and PLGA nanoparticles settled on the substrate. b. AFM topographical image of PLGA nanoparticles. c. Representative attractive F–D curves of positive QAβ-CD interacting with the negative PLGA surface. Red and black traces indicate retraction (detachment) signals of the AFM tip from a PLGA nanoparticle substrate and blank substrate, respectively. The five different force curves were produced from the same QAβ-CD-functionalized tip and are displaced vertically for clarity of presentation. d. Histogram (n = 110) of pull-off force values for the interaction of QAβ-CD with PLGA nanoparticles and blank substrates obtained with the same tip.

cantilever to adhere to nanoparticles beyond a certain distance (i), a distance where the tip was successfully separated from control substrates. It was not until after a certain point (ii) that adhesion was broken and the AFM tip was successfully separated from the nanoparticle surface. The average adhesion force between QAβ-CD and PLGA nanoparticles, as determined by force curves in Fig. 5c, was found to be approximately 8.5 ± 0.8 nN (Fig 5d). In contrast, the adhesion force measured using the same QAβ-CD-functionalized tip and a control surface containing no PLGA nanoparticles was found to be 0.4 ± 0.2 nN.

Force at the single molecule level was estimated using a technique called blind tip evaluation (40). The tip diameter was approximated as 8 nm after immersion in QAβ-CD solution, leading to the estimation that on the apex of the tip, 6-8 QAβ-CD molecules were present on the surface. Thus, the maximum force between a single QAβ-CD molecule and PLGA was determined to be 1.1 nN. In contrast, the maximum force between a single QAβ-CD molecule and the control surface was 59.2 pN. The adhesive force between QAβ-CD and PLGA proved extremely strong, especially when compared to biological interactions in nature. As an example, Hinterdorfer and coworkers reported that the single molecule force between IgG and single strand DNA was approximately 50 pN (41). The strong force between QAβ-CD and the PLGA surface is most likely a combination of ionic, Van der Waals, and molecular interaction forces. The firm adhesion between the core forming material and shell was hypothesized to contribute to pronounced stability of the nanoparticle upon intravenous infusion into the blood stream, preventing undesirable premature release of drugs prior to arrival at the tumor site.

Nested nanoparticle assembly and size and morphology characterization

Having verified the strong adhesion between core- and shell-forming components, the nested nanoparticle platform, comprising a drug-containing nanoparticle core coated with a shell composed of cyclodextrin-complexed drug (Fig. 6a), was fabricated and characterized. Throughout the entirety of the study, the fluorophores rhodamine and bodipy were used as model drugs for encapsulation within PLGA nanoparticles and complexation with QAβ-CD, respectively. For ease of platform morphological and architectural analysis, specifically core-shell compartmentalization of distinct drugs, rhodamine-containing PLGA microspheres averaging 2 μm in diameter were

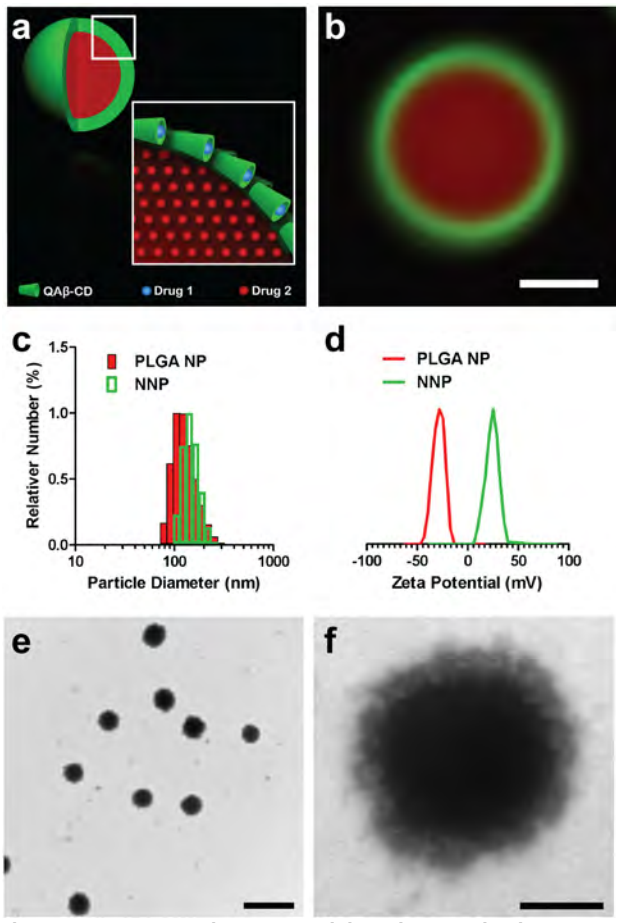

Figure 6. Nested nanoparticle characterization. a. Schematic of the proposed nested nanoplatform. b. Confocal microscopy image of a single nested particle demonstrating the core-shell compartmentalization of bodipy (green) and rhodamine (red). The scale bar represents 5 μm. c. Dynamic light scattering histogram depicting the size of nanoparticles prior to and after functionalization with the QAβ-CD shell. d. Zeta potential analysis of nanoparticles prior to and after addition of the QAβ-CD shell. e. Transmission electron microscopy image of nested nanoparticles. The scale bar represents 500 nm. f. Magnification of nested nanoparticle from e. The scale bar represents 100 nm.

fabricated and subsequently coated with bodipy-cyclodextrin complexes (bodipy•QAβ-CD). Upon examination of nanoparticles via confocal microscopy, rhodamine (red) encapsulated within the PLGA core and a bodipy•QAβ-CD shell (green) enveloping the nanoparticle were clearly discernible (Fig. 6b). As hypothesized, the outer drug layer formed a dense uniform coating around the nanoparticle, with distinct compartmentalization of the two drugs within the system.

The morphology and architecture achieved on the microscale was expected to effectively translate towards the nanoscale, a size range beneficial for both long-term circulation(42) and accumulation in tumors through the EPR effect (36). Rhodamine-containing PLGA nanoparticles possessed an average diameter of 105 nm as determined by dynamic light scattering (DLS) analysis (Fig. 6c). Upon addition of the bodipy•QAβ-CD outer shell, the size of the nanoparticles increased to an average diameter of 142 nm. Nested nanoparticle size and morphology were examined using scanning electron microscopy (SEM) and atomic force microscopy (AFM). As can be seen in Figure 7, nested nanoparticles were small in diameter, agreeing with the size of the nanoparticles as determined by dynamic light scattering. The SEM and AFM micrographs also depict the spherical shape of the nanoparticles, as well as the monodispersity of the sample. SEM and AFM examination demonstrated the small size and spherical morphology of nested nanoparticles, confirming their monodispersity (Figure 7). Analysis of the surface charge of the nanoparticles, prior to and following addition of the bodipy•QAβ-CD shell, confirmed the presence of the cyclodextrin outer layer. As is evident in Fig. 6d, the negative surface charge associated with PLGA nanoparticles (-28 mV) became highly positive (+25 mV) following the addition of bodipy•QAβ-CD. Successful assembly of the core-shell construct was further verified via TEM, which served to corroborate the small and uniform size of the nanoparticles (Fig. 6e).

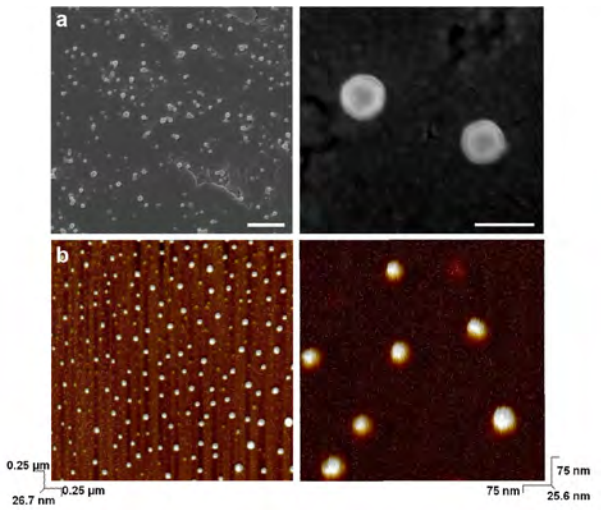

Figure 7. SEM and AFM examination of nested nanoparticles. a. SEM image of nested nanoparticles. The scale bar represents 1 µm. The figure immediately to the right is a magnification of the nanoparticles under SEM. The scale bar represents 200 nm. **b.** AFM image of nested nanoparticles, with the adjacent figure comprising a magnification of nanoparticles.

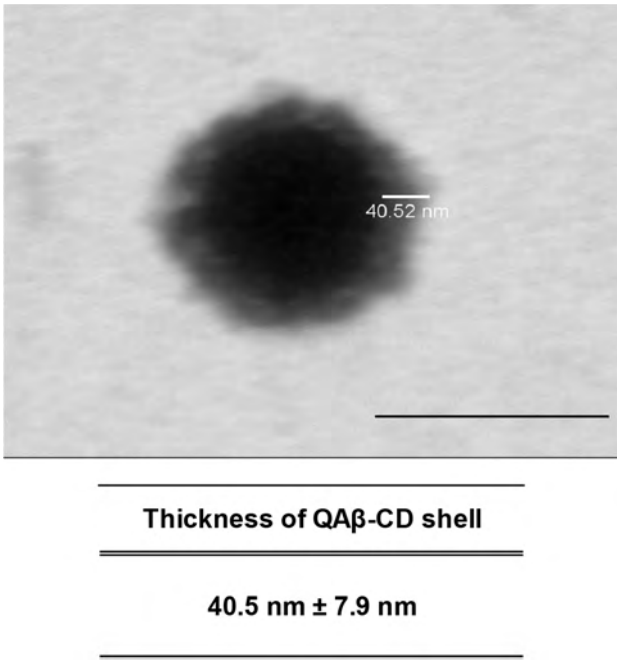

Figure 8. Cyclodextrin shell thickness quantification. TEM and ImageJ analysis used to determine the thickness of the cyclodextrin shell surrounding nested nanoparticles, which was found to average 40 nm.

Examination of nested nanoparticle QAβ-CD shell thickness

The thickness of the cyclodextrin (QAβ-CD) shell surrounding the nested nanoparticles was examined via transmission electron microscopy (TEM). Briefly, 8 radial measurements of 10 nanoparticles were obtained using ImageJ software. Figure 8 depicts a magnification of a representative nested nanoparticle, with a radial measurement conducted to determine the thickness of the cyclodextrin coating. The average thickness of the cyclodextrin shell around the nanoparticle was determined to be 40.5 ± 8 nm, well in agreement measurements obtained using dynamic light scattering.

Magnification of nested nanoparticles under TEM demonstrated the presence of an outer layer surrounding the electron dense mass of the PLGA nanoparticle. Upon subsequent analysis, the thickness of the shell was found to agree with measurements obtained by dynamic light scattering.

Release examination from nested nanoparticles

Figure 9 summarizes the release kinetics of rhodamine and bodipy from nested nanoparticles. As is evident in Fig. 9a, minimal drug release occurred from nanoparticles in the initial timepoints leading up to 3 h (7% and 3% of bodipy and rhodamine, respectively). Nominal release at early timepoints following intravenous administration should limit accumulation of drugs in healthy tissues and organs, in turn hindering potential side effects (43), and allowing sufficient time for the nanoparticle to successfully accumulate at the site of action prior to release. After 3 h, an increase in bodipy release occurred, reaching 34% of drug by 6 h. By 12 h, 50% of bodipy was released from nanoparticles, with release plateauing after 48 h. It is important to note that minimal release of rhodamine (~6%) occurred by this same timepoint. Indeed, throughout the entirety of the study, rhodamine release was extremely slow and sustained, reaching merely 34% release in 96 h.

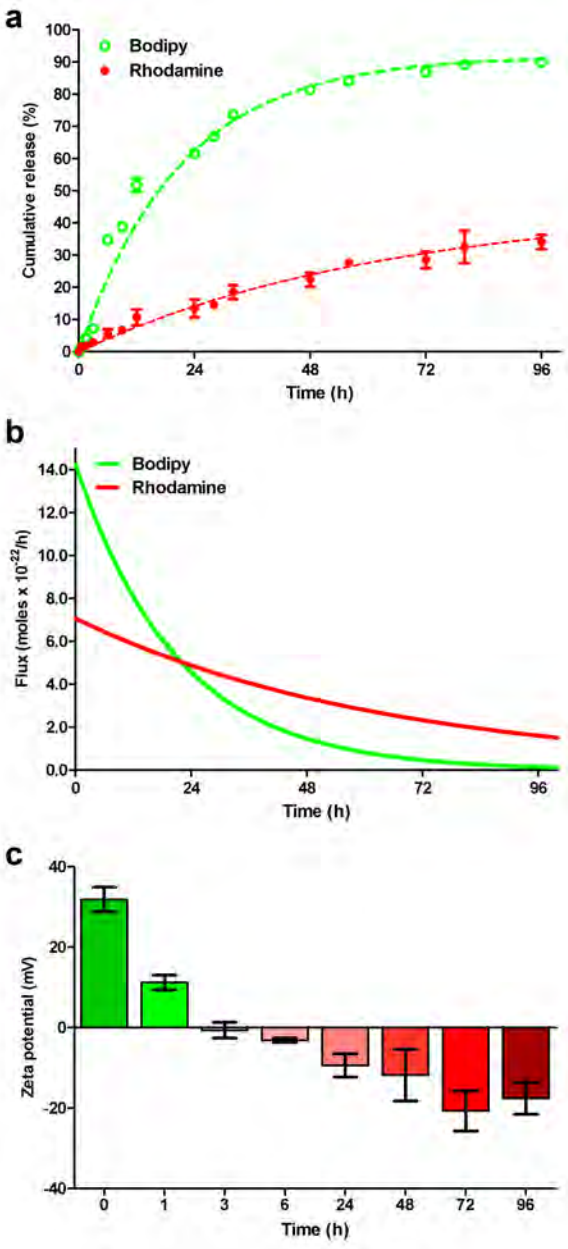

Figure 9. Examination of nested nanoparticle release kinetics. a. Cumulative release of bodipy and rhodamine from nested nanoparticles in PBS at pH 7.4 and 37ºC. Model fits to experimental data are represented by dotted lines. **b.** Fluxes of bodipy and rhodamine release from nested nanoparticles. **c.** Zeta potential examination of nested nanoparticles at specific timepoints in simulated release conditions (PBS at pH 7.4 and 37ºC).

Modeling of release kinetics

A Finite Element (FE) method was used to model drug diffusion. The model included partitioning conditions at the surfaces, in this case between the core and

the surrounding fluid. Due to the fact that the physico-chemical properties of the core and shell, as well as bodipy and rhodamine, are different, a computational method accounting for diffusivities and molecule partitioning was used to analyze release kinetics from nested nanoparticles. Thus, aside from the incremental-iterative system of mass balance equations (44-46):

$$\left(\frac{1}{\Delta t}\mathbf{M}+\mathbf{K}\right)\Delta\mathbf{C}^{(i)}=\mathbf{Q}^{ext}-\mathbf{Q}^{\mathrm{int}(i-1)}$$

we included the partitioning condition

$$\Delta N_s/\Delta N_f=\Delta C_s/\Delta C_f=P$$

Here, **M** and **K** are element mass and diffusion matrices, $\Delta\mathbf{C}$ represents nodal concentration increments, $\mathbf{Q}^{ext}$ and $\mathbf{Q}^{\mathrm{int}}$ are external and internal nodal mass fluxes; ΔN_s and ΔN_f are number of molecules of solid and fluid (per FE node) passing during time step Δt, and ΔC_s and ΔC_f are the corresponding concentration changes at boundary nodes with partitioning property; P is partitioning coefficient; and i specifies the equilibrium iteration counter. The important material parameter in the above balance equation is the diffusion coefficient D entering the diffusion matrix **K**:

$$K_{IJ}=\int_V D\left(\partial N_I/\partial x_j\,\partial N_J/\partial x_j\right)dV$$

where N_I , N_J are interpolation functions and V is element volume. This computational procedure was built into the FE package PAK(47).

The table below shows the parameters used to establish the model:

	Core	Shell	Units	Comments
R	52.5	70.5	nm	
d	-	18	nm	(shell thickness)
Mol.Mass	479	661	Da	
$C_{t=0}$	0.069	0.039	M	(initial molar concentration)
logP octanol/water)	319 (48)	0.013 (48)		(for comparison only:
D_{water}	$4\cdot10^{-6}$	$4\cdot10^{-6}$	cm^2/s	(diffusivity in water)
*D_{NP}	$D_{water}/5$	$D_{water}/10^4$	cm^2/s	(diffusivity inside material)
*Partitioning	$5\cdot10^9$	$2.2\cdot10^{11}$		(between water and solid material)
R^2	0.99	0.82		(square of Pearson's *r* between experiment and simulation)

* - values adopted to fit the experimental release.

The core composed of PLGA showed no significant degradation within the timeframe of experiments, and thus, diffusion was assumed to govern release of material. The shell composed of QAβ-CD was assumed to be either lost or degraded within or after a certain period

of release, where diffusion of bodipy alone or bodipy complexed with QAβ-CD was estimated to be similar in nature due to small differences of the final molecular size. The experimental diffusivity, D_{water}, was established for rhodamine ($4 \cdot 10^{-6}$ cm^2/s (49)), but was approximated for bodipy from previous literature (50). We also assumed that release from shell and core compartments did not substantially affect one another. Diffusivities inside the material (core and shell) were fitted together with partitioning coefficients P.

Use of the model helped determine that sequential release may be achieved and controlled not only by different diffusion properties in different phases, but also partitioning. Modeling results suggest that release from the core and shell saturated at 46% and 92%, respectively. The model estimated experimental release curves by using partitioning coefficients of 5.0×10^9 and 2.2×10^{11} for bodipy and rhodamine, respectively (Fig. 9a). The half-time of release of the maximum releasable material was estimated to be 15 h for the shell and 46 h for the core. The diffusivity of rhodamine inside the PLGA nanoparticle matrix was estimated to be 4×10^{-10} cm^2/s, which was approximately 10^4 times lower than that in water (49), while that of bodipy in the shell was reduced by only 5 times compared to that in water. Based on the model fit, the partitioning of both rhodamine and bodipy proved to be the most important factor influencing release kinetics, proving critical in the design of future embodiments of nested nanoparticles for sequential release. This is illustrated in the distinct phases of dominant fluxes over time (Fig. 9b). The rate of release of rhodamine from nested nanoparticles was initially outperformed by bodipy release, but eventually the rhodamine flux overtook the flux of bodipy after 24 h.

Nanoparticle surface charge examination at distinct timepoints provided valuable insights into the mechanism of drug release. As apparent in Fig. 9c, the nested nanoparticle platform was positively charged at the initial timepoints. However, as time progressed, the nanoparticle became less positive, with the surface charge undergoing an inflection and shift towards negative values after the 3 h timepoint. Noticeably, this coincided with the timeframe of increased release of bodipy observed in Fig. 9a. At subsequent times, the nanoparticle became increasingly negative, plateauing at roughly the same time as bodipy release. Taken together, the mechanism of release of bodipy from nested nanoparticles was driven primarily through detachment and displacement of cyclodextrin-complexed drug from nanoparticle surfaces. Slow release of rhodamine was primarily due to the high inherent viscosity of the PLGA polymer utilized in the study, shown previously to result in sustained release of therapeutics over time (51, 52), as well as partitioning that demonstrated preference of rhodamine molecules for the PLGA phase.

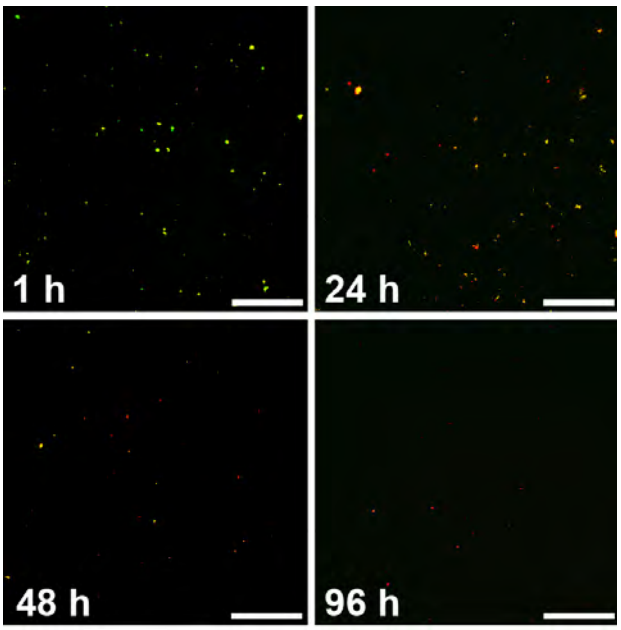

Figure 10. Confocal microscopy examination of release from nested nanoparticles. Confocal microscopy examination of nanoparticles at predetermined timepoints following incubation in PBS at pH 7.4. The green fluorescence emanates from bodipy while the red fluorescence from rhodamine. The scale bar represents 100 µm.

Confocal microscopy examination of drug release from nested nanoparticles

Confocal microscopy was used to obtain a qualitative visualization of drug release from nested nanoparticles in PBS 7.4 at 37ºC. At predetermined timepoints, nanoparticles were

removed from release media and examined using confocal microscopy. Results demonstrate that at short timepoints of 1 h, nanoparticles contained the bodipy•QAβ-CD shell surrounding the core, as evidenced by green fluorescence (Fig. 10). At 24 h, the population of nanoparticles containing bodipy decreased, and the rhodamine-containing core became apparent in nanoparticles. At later timepoints of 48 and 96 h, the bodipy cyclodextrin shell became disassociated from the nanoparticles, resulting in rhodamine-containing nanoparticles (red fluorescence).

Cytotoxicity evaluation of nested nanoparticles

Potential cytotoxic effects stemming from the nested nanoparticle platform were examined in human primary endothelial cells via MTT assay. As can be appreciated in the accompanying figure (Figure 11), nested nanoparticles did not prove overtly cytotoxic over the range of doses examined. Toxicity was absent at low doses, and cell viability was affected at higher doses, with toxicity stemming from nested nanoparticles correlating directly with that observed with PLGA controls at these same doses.

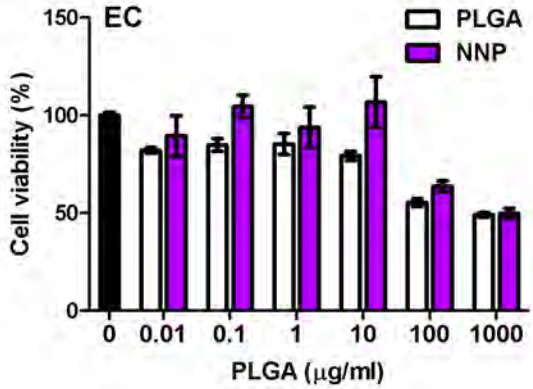

Figure 11. Cytotoxicity examination, via MTT assay, in human primary endothelial cells following 24 h incubation with nested nanoparticles and control PLGA nanoparticles at varying doses.

Examination of nested nanoparticle internalization and intracellular sequential release within breast cancer cells

Nanoparticle internalization and subsequent intracellular localization and drug release were examined in MCF-7 breast cancer cells (Fig. 12). As can be observed in confocal micrographs comprising Fig. 12a, nested nanoparticles underwent internalization in MCF-7 breast cancer cells after 1 h of incubation. Internalization of nested nanoparticles was likely facilitated by their positive surface charge, which has been previously shown to enhance traversal through negatively-charged membranes via endocytotic pathways (53, 54). Intracellular release of drugs over time was evident, with fluorescence of bodipy waning as time progressed past the 3 h timepoint. At later timepoints of 24 and 96 h, the fluourescence emanating from MCF-7 cells was primarily due to rhodamine in nanoparticles, with the majority of bodipy

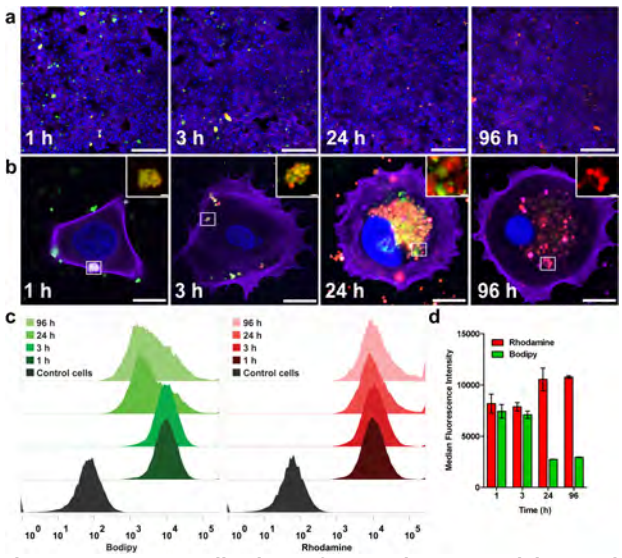

Figure 12. Internalization of nested nanoparticles and intracellular release in MCF-7 breast cancer cells. a. Confocal microscopy of MCF-7 breast cancer cells at predetermined timepoints after administration of nested nanoparticles. The green fluorescence emanates from bodipy while the red fluorescence from rhodamine. The scale bar represents 100 μm. **b.** Single-cell confocal microscopy examination of nested nanoparticle internalization and release at different timepoints. Green fluorescence is due to bodipy while red fluorescence denotes the presence of rhodamine. The scale bar represents 40 μm. Figure insets represent magnifications of areas outlined in boxes. The scale bars in the insets represent 2 μm. **c.** Flow cytometry histograms of nanoparticle accumulation over time in MCF-7 breast cancer cells. **d.** Mean fluorescence intensity over time in MCF-7 breast cancer cells as determined by flow cytometry analysis.

having been released.

Single-cell analysis (Fig. 12b) provided further insights into nested nanoparticle internalization and release, as well as intracellular trafficking. By 1 h, nanoparticles have undergone association with the cell membrane, and were shown to undergo engulfment in early endosomes. At later timepoints, larger amounts of nanoparticles were internalized, leading to the formation of larger, late-stage endosomal compartments. As can be seen at timepoints of 24 and 96 h, migration of nanoparticles to the perinuclear region of the cell has occurred, with nanoparticles likely found within lysosomal bodies. Analagous to Fig. 12a, bodipy and rhodamine were found to be co-localized and associated with nanoparticles at early timepoints, while at later timepoints, only rhodamine fluorescence remained, successfully demonstrating intracellular sequential drug release dynamics using the nested nanoparticle platform.

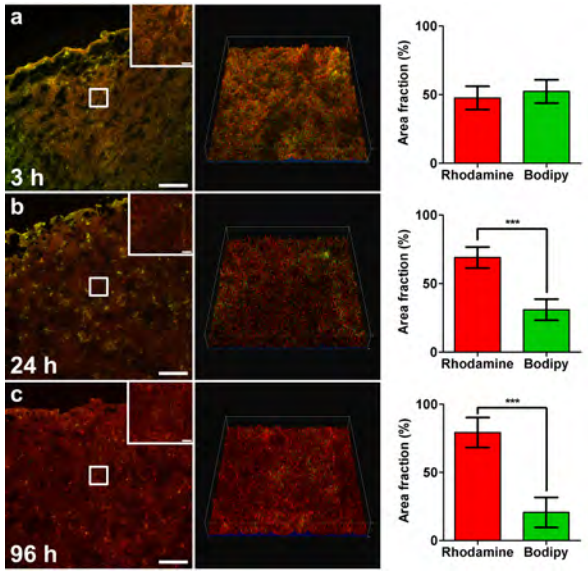

Figure 13. Nested nanoparticle accumulation in an MCF-7 murine model of breast cancer. a., b., and **c.** comprise representative confocal microscopy images of excised MCF-7 tumors at 3, 24, and 96 h, respectively. Green fluorescence is due to bodipy while red fluorescence denotes the presence of rhodamine. The scale bars in the images represent 100 µm. Immediately to the right of each confocal microscopy image is a fluorescence intensity plot of boxed areas in the preceding figure. The last column of the figure represents area of bodipy and rhodamine as a fraction of the total area, plotted as the percentage of fluorophore content in tumors (n = 3), obtained from multiple tissue slices at their corresponding timepoints. Asterisks (***) indicate a significance level of $p < 0.001$.

Intracellular release behavior was quantified utilizing flow cytometry analysis. As shown in Fig. 12c and 12d, the intracellular fluorescence intensity of bodipy decreased significantly after 24 h, confirming the sequential release behavior of the nanoparticles. Contrastingly, and in agreement with in vitro and cellular studies, the release of rhodamine did not vary significantly over time, demonstrating slow and sustained release dynamics.

In vivo examination of sequential release from nested nanoparticles

Nested nanoparticles were designed to successfully navigate the bloodstream following intravenous administration and site-specifically accumulate in tumors, releasing its contents in a time- and sequence-dependent fashion (Fig. 1). MCF-7 breast tumor xenografts from mice were examined for the presence of bodipy and rhodamine using confocal microscopy at different timepoints following administration. As can be seen in Fig 13a, tumor tissues show colocalization of both dyes 3 h after administration of nested nanoparticles. Surface intensity plots (Fig 13a) clearly highlight bodipy and rhodamine fluorescence, indicating accumulation of nanoparticles within the tumor at this relatively short timepoint. Importantly, these findings reinforce the stability of the nanoparticle construct following intravenous administration. Area fraction analysis of distinct regions of the tumor demonstrated that bodipy and rhodamine were found in ratiometrically similar amounts within the tumor at 3 h. In contrast, at 24 h, there was a marked decrease of bodipy in the tumor tissue (Fig. 13b), as reflected in the accompanying surface intensity plot and area fraction analysis. At 96 h, confocal micrographs show that the vast majority of the tumor tissue examined emanated rhodamine-associated fluorescence, with minimal bodipy fluorescence in the tumor (Fig. 13c). Area fraction analysis demonstrated an increase in rhodamine amount at this time in the tumor, while the amount of bodipy in the tumor has decreased significantly. Taken together, these results demonstrate that the nested

nanoparticle platform is capable of sequential release intratumorally. Importantly, the slow intratumoral release of drug from the nanoparticle core observed in these studies may prove beneficial, as improved tumor efficacies have been observed following prolonged exposure to therapeutics (19).

Sequence delivery of therapeutics for enhanced synergistic antitumor efficacy in triple negative breast cancer cells

Previously, delivery of rapamycin and paclitaxel to triple negative breast tumors provided valuable insights into the mechanism of synergy enhancement involving suppression of feedback loop Akt phosphorylation. Consequently, this led to inhibition of several downstream targets of Akt, including PRAS40, Bad, GSK3β, as well as S6K and S6, the downstream targets of mTOR. Synergy between rapamycin and paclitaxel has been explored preclinically in several different cancers (7, 55, 56), and clinically in several completed (57, 58) and ongoing trials, with the precise mechanism remaining elusive. The initial rationale for synergy was sound, with reports pointing to the role of mTOR as a cell survival protein (7) and Akt activation after paclitaxel treatment causing resistance to the drug (59, 60). However, rapamycin was also reported to activate Akt through negative feedback loop activation (61-63). Results indicated that pAkt is indeed increased following rapamycin treatment. However, co-administration of low dose paclitaxel with rapamycin was not associated with a statistically significant increase in pAkt, and inhibited activation of PRAS40, itself an inhibitor of

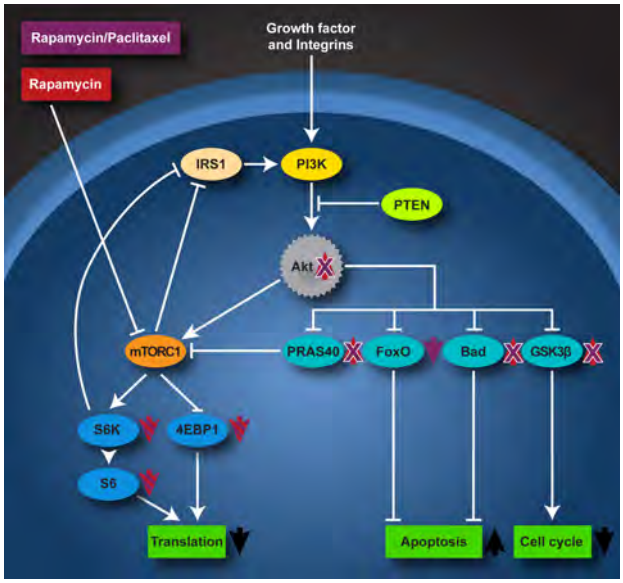

Figure 14. **Rapamycin and paclitaxel synergistically target the PI3K/Akt/mTOR pathway by suppressing feedback loop Akt phosphorylation**. Rapamycin treatment alone causes a decrease in phosphorylated S6 and S6K, as well as 4E-BP1, and an increase in pAkt through feedback loop activation. Rapamycin and paclitaxel also result in a decrease in phosphorylated S6, S6K, and 4E-BP1, but result in a decrease in pAkt. Combination therapy also inhibited phosphorylation of PRAS40, Bad, and GSK3β, all previously shown to increase with rapamycin treatment alone. Concomitant delivery also showed a decrease in phosphorylation of FoxO proteins.

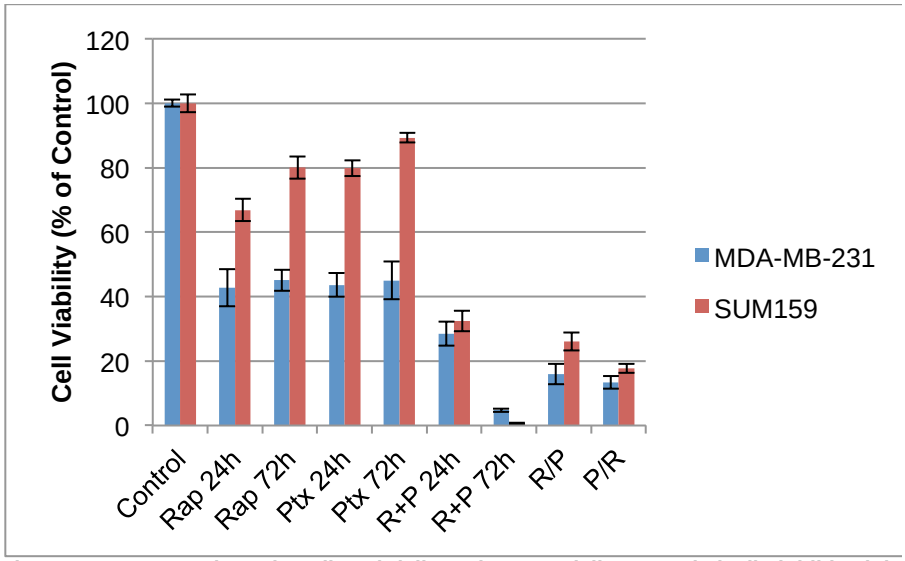

Figure 15. **Rapamycin and paclitaxel delivered sequentially synergistically inhibit triple negative breast cancer cell growth**. Rapamycin and paclitaxel were administered to MDA-MB-231 and SUM-15 breast cancer cells at different times and in different sequences, and growth inhibition was assessed via MTT assay. R+P signifies drug administered concomitantly, while R/P means sequential and with a timed difference.

mTOR, and GSK3β, a key protein involved in cellular proliferation, as well as Bad and the FoxO family, proteins involved in apoptosis (Fig. 14). One of the reasons for inhibition of Akt activation by paclitaxel is possibly related to nuclear translocation of FoxO3a by paclitaxel (64). These findings provided the rationale for introducing both paclitaxel (a well established chemotherapeutic) and rapamycin (a repositioned, molecular-targeted agent) within the nested nanoparticle platform, in attempts to hinder pro-survival feedback loop activation associated with rapamycin administration.

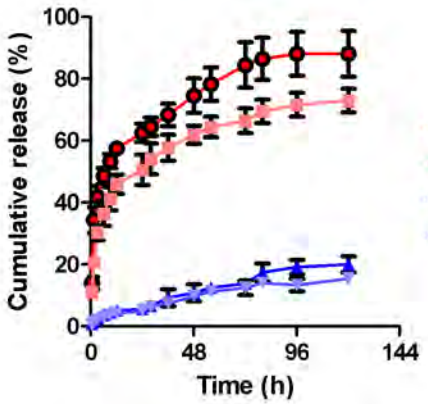

Figure 16. **Rapamycin and paclitaxel release from nested nanoparticles in a time and sequential fashion.** Rapamycin was incorporated within the outer cyclodextrin shell while paclitaxel was incorporated within the core of nanoparticles. Release was examined at pH 5.0 and 7.4 at 37ºC, and at predetermined timepoints, drug released was assayed via HPLC.

We first examined the efficacy of sequentially administering rapamycin and paclitaxel to SUM159 and MDA-MB-231 triple-negative breast cancer (TNBC) cells, all with the eventual hope of introducing both of these agents in the nested nanoparticle platform. An MTT assay was performed where rapamycin and paclitaxel were administered in different sequences and during different administration times. As can be seen in Fig. 15, sequential administration of rapamycin and paclitaxel indeed proved effective at inhibiting SUM 159 and MDA-MB-231 TNBC cell growth. Of significant note, rapamycin administered 24 h prior to paclitaxel proved exceptionally effective at growth inhibition, and proved to be compatible with loading of the drugs within their respective compartments (rapamycin complexed with cyclodextrin and paclitaxel housed within PLGA nanoparticles). This order of sequence, rapamycin administration prior to paclitaxel, was maintained throughout the course of subsequent *in vitro* and *in vivo* evaluation.

Sequential release of rapamycin and paclitaxel from nested nanoparticles

Following *in vitro* efficacy examination of rapamycin and paclitaxel in triple negative breast cancer cells, paclitaxel and rapamycin were incorporated within the nested nanoparticle and the release kinetics of the drugs were evaluated. Similar to the findings discussed previously, the nested nanoparticle platform proved capable of delivering drugs in a time and sequence fashion. As can be observed in Fig. 16, release of rapamycin from nested nanoparticles occurred at a faster rate than paclitaxel. Within the first 24 h, approximately 60% of the drug was released from nanoparticles compared to less than 10% release of paclitaxel within the same time frame. After 4 d in release media, >80% of rapamycin was released from nanoparticles, while paclitaxel release had not yet achieved 20%. The rapid release kinetics of rapamycin from should immediately inhibit cell growth through efficient knockdown of pS6. The sustained release of paclitaxel should inhibit rapamycin-induced feedback loop activation, as well as act as a drug-eluting depot capable of providing long-term tumor growth suppression.

In vitro *antitumor efficacy evaluation in TNBC*

The growth inhibitory efficacy of the nested nanoparticle platform was then examined in SUM-159 triple negative breast cancer cells *in vitro* (Fig. 17). Following 4 d incubation, free drug formulations of rapamycin and paclitaxel, as well as a sequential combination of these proved highly efficacious at inhibiting breast cancer cell growth. By comparison, PTX nanoparticles were incapable of inhibiting breast cancer cell growth following administration. This is most likely due to differences in uptake mechanisms between free drug formulations and

nanoparticles, as well as the fact that the drug is released in a much more prolonged and sustained fashion from nanoparticles. It is important to note that the SUM-159 breast cancer cell line is sensitive to the growth inhibitory effects of rapamycin, therefore explaining the increased growth inhibition observed with rapamycin and cyclodextrin complexes. The nested nanoparticle formulation of paclitaxel and rapamycin proved highly effective at inhibiting breast cancer growth during this time. This is likely the result of enhanced internalization of nested nanoparticles into cells (owing to the net positive charge of nanoparticles) followed by the effects of the rapid release of rapamycin and prolonged release of paclitaxel.

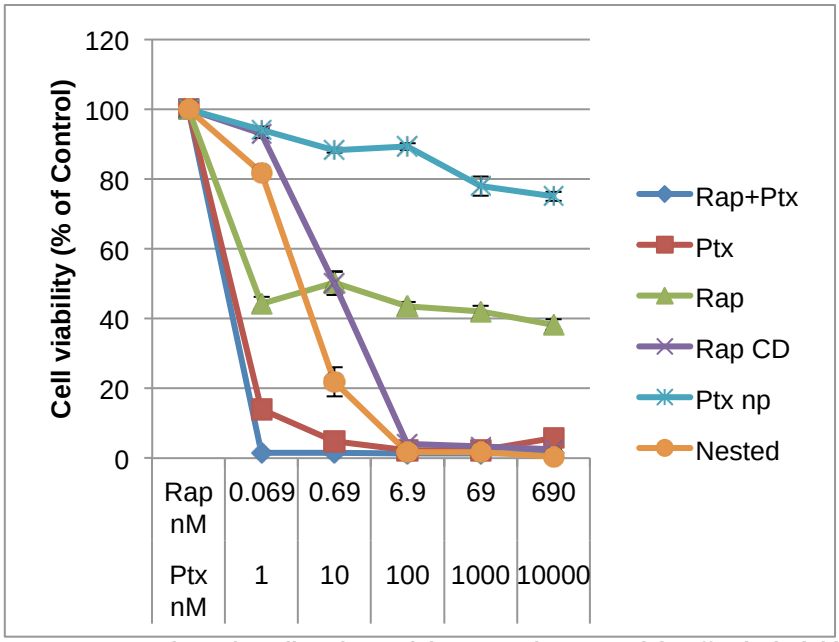

Figure 17. **Rapamycin and paclitaxel-containing nested nanoparticle effectively inhibited SUM-159 breast cancer growth *in vitro*.** Rapamycin was incorporated within the outer cyclodextrin shell while paclitaxel was incorporated within the core of nanoparticles. Release was examined at pH 5.0 and 7.4 at 37ºC, and at predetermined timepoints, drug released was assayed via HPLC.

In vivo efficacy evaluation in murine models of TNBC

The antitumor efficacy of the nested nanoparticle platform was then examined in a murine model of triple negative breast cancer (Fig. 18). Female nude mice were inoculated with SUM-159 triple negative breast tumors in the mammary fat pad, and received nested nanoparticles once a week for the duration of 3 weeks. As can be observed from the figure, control tumors grew rapidly over the course of treatment, reaching an approximate tumor volume of 1000 mm3 by the end of treatment. Paclitaxel nanoparticles were incapable of suppressing tumor growth, as was the case with rapamycin administered in cyclodextrin form. Contrastingly, nested nanoparticles proved highly efficacious with regards to tumor growth

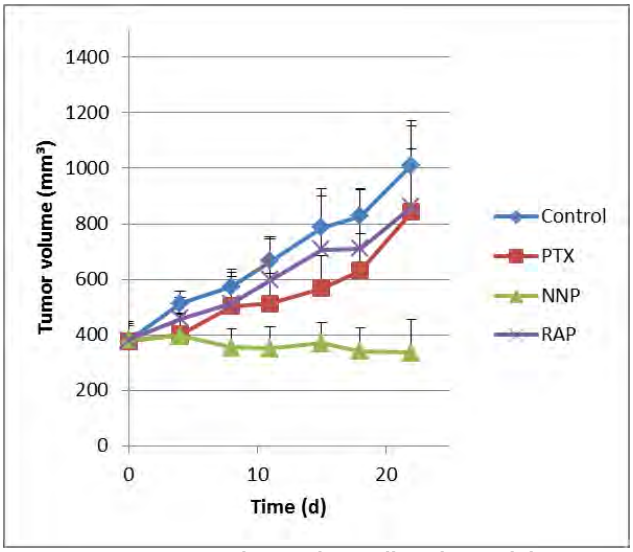

Figure 18. **Rapamycin and paclitaxel-containing nested nanoparticles effectively suppress SUM-159 breast cancer growth *in vivo*.** Nested nanoparticles were administered to female nude mice bearing SUM-159 breast tumors. Treatments were administered once a week for the duration of 3 weeks, during which, tumor volume was evaluated via caliper measurements at predetermined timepoints.

inhibition, resulting in a decrease in tumor volume compared to the initial starting volume. This is most likely due to the site-specific synergistic enhancement provided by the sequential release of rapamycin and paclitaxel in tumors.

To confirm the synergistic mechanism of action, western blot assays were conducted on excised tumors at the end of the duration of treatment (Fig. 19). As can be observed in the figure, rapamycin treatment resulted in an increase in pAkt, confirming the previously mentioned feedback loop activation that results in cell survival. Rapamycin was also capable of suppressing pS6 compared to paclitaxel treatment. Of significant note, nested nanoparticles were capable of inhibiting pAkt activation compared to rapamycin controls, all the while significantly suppressing pS6 compared to all control groups, possibly serving to explain the exceptional antitumor effect of the nested nanoparticles that resulted in regression.

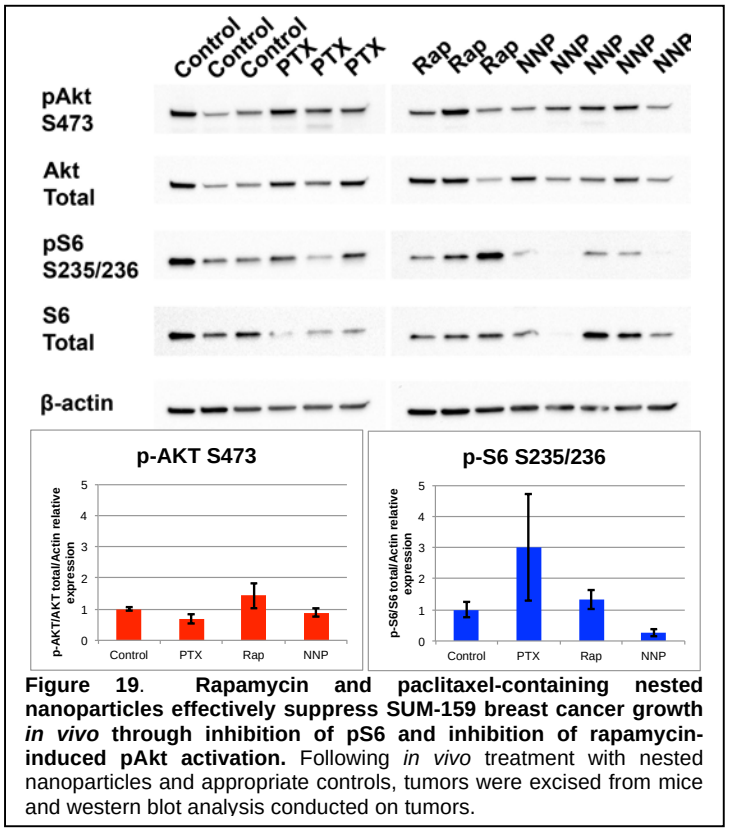

Figure 19. Rapamycin and paclitaxel-containing nested nanoparticles effectively suppress SUM-159 breast cancer growth *in vivo* through inhibition of pS6 and inhibition of rapamycin-induced pAkt activation. Following *in vivo* treatment with nested nanoparticles and appropriate controls, tumors were excised from mice and western blot analysis conducted on tumors.

Key Research Accomplishments

- Fabricated PLGA polymer nanoparticles with a net negative charge on the surface highly capable of binding an outer positively-charged shell through electrostatic binding – Task 1, Specific Aim 1
- Optimized fabrication of core-forming nanoparticles to produce smaller sized (~100 nm), monodisperse nanoparticles – Task 1, Specific Aim 1
- Characterized nanoparticles using scanning electron microscopy, dynamic light scattering, fluorescence microscopy, and UV-Vis spectroscopy – Task 1, Specific Aim 1
- An outer shell consisting of quaternary ammonium cyclodextrins was stably grafted electrostatically to the outer surface of PLGA particles – Task 2, Specific Aim 2
- Verified the high electrostatic binding efficiency between the positively-charged cyclodextrin outer shell and the negatively-charged PLGA nanoparticle via AFM - Task 2, Specific Aim 1
- Characterized and verified successful formation of ~150 nm nested nanoparticles using scanning electron microscopy and atomic force microscopy (size and morphology verification), transmission electron microscopy (morphology, size, core/shell architecture verification), and zeta potential analysis (core/shell architecture) – Task 2, Aim 1
- Demonstrated, via confocal microscopy, the formation of core-shell morphology of nested nanoparticles, wherein separate drugs can be incorporated in distinct regions (i.e. core and shell) for purposes of sequential release – Task 2, Specific Aim 1
- Of significant importance, results demonstrate the sequential release of model drugs from the nested nanoparticle platform – Task 2, Specific Aim 1

- Sequential release of agents from the nested nanoparticle platform was simulated based on mathematical models – Task 2, Specific Aim 1
- Nested nanoparticles were shown to internalize within both MCF-7 and SUM159 breast cancer cells, and examination of single cells using confocal microscopy showed preservation of release kinetics observed in *in situ* conditions – Task 2, Aim 1
- Of significant importance, nested nanoparticles were shown to accumulate in tumors, where sequential release of agents was demonstrated over time – Task 2, Aim 1
- Rapamycin and paclitaxel were shown to act synergistically in a time and sequence fashion when rapamycin is given 24 h prior to paclitaxel – Task 1, Aim 2
- Constituent components, the paclitaxel-containing PLGA nanoparticle (core) and the rapamycin cyclodextrin complex (outer shell), were successfully combined, yielding drug-containing nested nested nanoparticles – Task 2, Aim 1
- Examined the release kinetics of rapamycin and paclitaxel from nested nanoparticle platform in *in vitro* conditions – Task 2, Aim 1
- Cytotoxicity of the nested nanoparticle platform alone was shown to not affect cell viability compared to PLGA nanoparticles alone in human primary endothelial cells – Task 1, Aim 2
- Examined the cell killing effect of the nested nanoparticle platform in triple negative breast cancer cells *in vitro* using MTT cell proliferation assay – Task 1, Aim 2
- Efficacy of the nested nanoparticle platform was examined in murine models of triple negative breast cancer, demonstrating exceptional antitumor growth inhibition – Task 2, Aim 2
- Verified the mechanism of synergy of the nested nanoparticle platform *in vivo* using western blot analysis, effectively demonstrating suppression of pro-survival rapamycin-induced feedback loop activation – Task 2, Aim 2

Reportable Outcomes

- Refereed publications
    - Ruiz-Esparza, G.U.; Wu, S.; Segura-Ibarra, V.; Cara, F.E.; Evans, K.W.; Milosevic, M.; Ziemys, A.; Kojic, M.; Meric-Bernstam, F.; Ferrari, M.; Blanco, E. Polymer nanoparticles encased in a cyclodextrin complex shell for potential site- and sequence-specific drug release. *Adv Funct Mater*, 2014, 24, 4753-4761.
      **Featured as a cover image*
    - Choi, D.S.;* Blanco, E.;* Kim, Y.S.; Rodriguez, A.A.; Zhao, H.; Huang, T.H.; Chen, C.L.; Jin, G.; Landis, M.D.; Burey, L.A.; Qian, W.; Granados, S.M.; Dave, B.; Wong, H.H.; Ferrari, M.; Wong, S.T.; Chang, J.C. Chloroquine eliminates cancer stem cells through deregulation of Jak2 and DNMT1. *Stem Cells*, 2014, 32, 2309-23.
      *Contributed equally
    - Blanco, E.; Sangai, T.; Wu, S.; Hsiao, A.; Ruiz-Esparza, G.U.; Gonzalez-Delgado, C.A.; Cara, F.E.; Granados-Principal, S.; Evans, K.W.; Akcakanat, A.; Wang, Y.; Do, K.A.; Meric-Bernstam, F.; Ferrari, M. Colocalized Delivery of Rapamycin and Paclitaxel to Tumors Enhances Synergistic Targeting of the PI3K/Akt/mTOR Pathway. *Mol Ther*, 2014, 22, 1310-19.
    - Blanco, E.; Ferrari M. Emerging nanotherapeutic strategies in breast cancer. *Breast* 2014, 23,10-8.
    - Ruiz-Esparza, G.U.; Flores-Arredondo, J.H.; Segura-Ibarra, V.; Torre-Amione, G.; Ferrari, M; Blanco, E;* Serda, R.E.* The physiology of cardiovascular disease and innovative liposomal platforms for therapy. *Int J Nanomedicine*, 2013, 8, 629-40.
      **Shared senior authorship*

- Blanco, E.; Sangai, T.; Hsiao, A.; Ferrati, S.; Bai, L.; Liu, X.; Meric-Bernstam, F.; Ferrari, M. Multistage Delivery of Chemotherapeutic Nanoparticles for Breast Cancer Treatment. *Cancer Lett*, 2013, 334, 245-52.
- Blanco, E.; Hsiao, A.; Ruiz-Esparza, G.U.; Landry, M.G.; Meric-Bernstam, F.; Ferrari, M. Molecular-targeted nanotherapies in cancer: enabling treatment specificity. *Mol Oncol*, 2011, 5(6), 492-503.
  **Featured as a cover image*
- Huan, M.; Xing, G.; Blanco, E.; Wang, P.C.; Liang, X.; Li, X.; Song, Y.; Chen, C.; Sun, B.; Yuan, H.; Zhao, F.; Chen, Z.; Sun, T.; Chai, Z.; Ferrari, M.; Zhao, Y. Metallofullerene Nanoparticles for Fibrous Imprisonment of Tumors. *Nanomedicine*, 2012, 8, 136-146.
  **Featured as a cover image*
- Blanco, E.; Hsiao, A.; Mann, A.P.; Meric-Bernstam, F.; Ferrari, M. Nanomedicine in cancer therapy: innovative trends and prospects. *Cancer Sci*, 2011, 102, 1247-1252.
  **Featured as a cover image*
- Serda, R.E.; Blanco, E.; Mack, A.; Stafford, S.J.; van de Ven, A.L.; Tanaka, T.; Amra, S.; Li, Q.; Torchilin, V.; Wiktorowicz, J.E.; Ferrari, M. Proteomic Analysis of Serum Opsonins Impacting Biodistribution and Cellular Association of Porous Silicon Microparticles. *Mol Imaging,* 2011, 10, 43-55.
- Serda, R.E.; Godin, B.; Blanco, E.; Chiappini C.; Ferrari, M. Multi-Stage Delivery Nano-Particle Systems for Therapeutic Applications. *Biochim. Biophys. Acta,* 2011, 10, 317-29.Meeting abstracts and presentations

- Meeting abstracts and presentations
  - Blanco, E.; Sangai T.; Hsiao, A.; Ruiz-Esparza, G.U.; Meric-Bernstam F.; Ferrari M. Site-Specific, Concomitant Delivery of Rapamycin and Paclitaxel in Breast Cancer: Consequent Synergistic Efficacy Enhancement. 35th Annual San Antonio Breast Cancer Symposium 2012. December 4-8, 2012. San Antonio, TX. Abstract # P6-11-03.
  - Blanco, E.; Sangai T.; Hsiao, A.; Ferrati, S.; Bai, L.; Liu, X.; Meric-Bernstam F.; Ferrari M. Multistage Delivery of Paclitaxel: Increased Drug Stability and Sustained Release in Results in Enhanced Efficacy in Breast Cancer. 35th Annual San Antonio Breast Cancer Symposium 2012. December 4-8, 2012. San Antonio, TX. Abstract # P6-11-11.
  - Invited lecture (Elvin Blanco) at Swansea University (Wales, UK) entitled "Nanotherapeutic Synergy Enhancement in Triple Negative Breast Cancer and other Diseases." (August 2012)
  - Blanco, E.; Sangai, T.; Hsiao, A.; Meric-Bernstam, F.; Ferrari, M. Synergistic Delivery of PI3K-mTOR Chemotherapeutics with the use of Nanomedicine Platforms. Era of Hope Meeting for the Department of Defense (DOD) Breast Cancer Research Program. August 2-5, 2011. Orlando, FL. Abstract #P43-20.
  - Blanco, E.; Sangai, T.; Hsiao, A.; Chislett, S.P.; Martinez, J.O.; Ferrati, S.; Meric-Bernstam, F.; Ferrari, M. Chemotherapeutic-containing polymer micelle delivery in a multistage fashion using mesoporous silicon particles. AACR Nano in Cancer: Linking Chemistry, Biology, and Clinical Applications In Vivo. January 12-15, 2011. Miami, Florida. Abstract # 3.

- Fellowships/Grants

- NIH/NCI Clinical Loan Repayment Program (LRP) Award to Elvin Blanco (Renewal)

- Mentoring
  - Guillermo U. Ruiz-Esparza, an MD/PhD mentored by Elvin Blanco will defend his thesis Oct. 2014

- Employment
  - Dr. Suhong Wu has joined the laboratory as a postdoctoral researcher playing an instrumental role in the design and development of the nested nanoparticle platform
  - Victor Segura-Ibarra, an MD/PhD student, has joined the laboratory and is involved in the eventual translation of the nanoparticle platform for therapeutic purposes

Conclusion

Site-specific delivery of multiple drugs is of paramount importance in cancer, where combination chemotherapy regimens aim to exploit synergistic cell-killing efficiency while minimizing drug resistance and adverse patient side effects. Nanoparticle-based drug delivery has successfully overcome pharmacokinetic limitations of conventional drug formulations, aptly navigating intricate biological barriers to co-deliver therapeutics to tumors. However, novel insights into molecular mechanisms governing tumorigenesis extend the notion of synergistic enhancement to order and timing of drug presentation (5, 7). In this proposed work, we have successfully developed a nanoparticle platform capable of site-specifically delivering drugs to tumors in a time- and sequence-dependent manner. We have demonstrated the formation of a highly stable nanoconstruct with sequential release behavior *in vitro*, a behavior that was effectively translated and preserved in cellular and *in vivo* models of breast cancer. We demonstrated the consequent synergistic efficacy of administering two drugs (rapamycin and paclitaxel) in a sequential manner, and incorporated these two in a platform capable of site-, time-, and sequence-based delivery, demonstrating not only efficacy in relevant murine models of triple negative breast cancer, but also preservation of synergistic mechanisms of action.

To the best of our knowledge, this is the first demonstration of intracellular and intratumoral sequential release of agents from a nanoparticle platform designed specifically for staggered release, highlighting the feasibility of the nanoparticle as a novel strategy for synergistic enhancement in cells necessitating chemosensitization, or as an approach to overcome feedback loop activation by pro-survival molecules. The findings presented herein represent the culmination of the development of a nested nanoparticle platform designed specifically for sequential release of therapeutics. Future work will be devoted to identification of potential synergistic avenues in cancer that might benefit from time- and sequence-dependent delivery of therapeutics, as well as other potential drug candidates for incorporation within the nanoparticle platform. We wish to extend this platform to a broad range of drug candidates that can result in enhanced synergy in a time- and sequence-specific fashion, and are confident that this platform will result in a more efficacious and personalized therapeutic modality for the treatment of breast cancer.

References

1. R. Siegel, D. Naishadham, A. Jemal, *CA Cancer J Clin* **62**, 10 (Jan, 2012).

2. D. J. Butters, D. Ghersi, N. Wilcken, S. J. Kirk, P. T. Mallon, *Cochrane Database Syst Rev*, CD003368 (2010).
3. D. Miles, G. von Minckwitz, A. D. Seidman, *The oncologist* **7 Suppl 6**, 13 (2002).
4. E. Blanco *et al.*, *Molecular oncology* **5**, 492 (Dec, 2011).
5. M. J. Lee *et al.*, *Cell* **149**, 780 (May 11, 2012).
6. N. McCarthy, *Nat Rev Cancer* **12**, 449 (Jul, 2012).
7. W. H. Mondesire *et al.*, *Clin Cancer Res* **10**, 7031 (Oct 15, 2004).
8. E. Calvo, V. Bolos, E. Grande, *Onco Targets Ther* **2**, 135 (2009).
9. H. Carraway, M. Hidalgo, *Breast Cancer Res* **6**, 219 (2004).
10. F. Meric-Bernstam, A. M. Gonzalez-Angulo, *J Clin Oncol* **27**, 2278 (May 1, 2009).
11. A. S. Fung, L. Wu, I. F. Tannock, *Clin Cancer Res* **15**, 5389 (Sep 1, 2009).
12. K. A. Janes, H. C. Reinhardt, M. B. Yaffe, *Cell* **135**, 343 (Oct 17, 2008).
13. K. Galoian, H. T. Temple, A. Galoyan, *Tumour biology : the journal of the International Society for Oncodevelopmental Biology and Medicine* **33**, 885 (Jun, 2012).
14. A. Hamilton *et al.*, *Annals of oncology : official journal of the European Society for Medical Oncology / ESMO* **13**, 910 (Jun, 2002).
15. A. Sparreboom *et al.*, *Clinical Cancer Research* **11**, 4136 (June 1, 2005, 2005).
16. L. D. Mayer *et al.*, *Molecular cancer therapeutics* **5**, 1854 (Jul, 2006).
17. A. Gabizon, H. Shmeeda, Y. Barenholz, *Clinical Pharmacokinetics* **42**, 419 (2003).
18. W. J. Gradishar, *Expert Opinion on Pharmacotherapy* **7**, 1041 (2006).
19. M. E. Davis, Z. G. Chen, D. M. Shin, *Nature reviews. Drug discovery* **7**, 771 (Sep, 2008).
20. M. Ferrari, *Nat Rev Cancer* **5**, 161 (Mar, 2005).
21. D. Peer *et al.*, *Nature nanotechnology* **2**, 751 (Dec, 2007).
22. H. Wang *et al.*, *Biomaterials* **32**, 8281 (Nov, 2011).
23. X. Dong *et al.*, *Cancer research* **69**, 3918 (May 1, 2009).
24. E. J. Feldman *et al.*, *J Clin Oncol* **29**, 979 (Mar 10, 2011).
25. J. R. Hasenstein *et al.*, *Molecular cancer therapeutics* **11**, 2233 (Oct, 2012).
26. Z. J. Deng *et al.*, *ACS nano*, (Oct 21, 2013).
27. S. Sengupta *et al.*, *Nature* **436**, 568 (Jul 28, 2005).
28. E. Tasciotti *et al.*, *Nature nanotechnology* **3**, 151 (Mar, 2008).
29. F. Danhier *et al.*, *Journal of controlled release : official journal of the Controlled Release Society* **161**, 505 (Jul 20, 2012).
30. J. K. Vasir, V. Labhasetwar, *Adv Drug Deliv Rev* **59**, 718 (Aug 10, 2007).
31. M. E. Davis, M. E. Brewster, *Nature reviews. Drug discovery* **3**, 1023 (Dec, 2004).
32. T. Loftsson, M. E. Brewster, *J Pharm Sci-Us* **101**, 3019 (Sep, 2012).
33. V. J. Stella, Q. He, *Toxicologic pathology* **36**, 30 (Jan, 2008).
34. R. A. Jain, *Biomaterials* **21**, 2475 (Dec, 2000).
35. F. Qian, N. Nasongkla, J. Gao, *J Biomed Mater Res* **61**, 203 (Aug, 2002).
36. H. Cabral *et al.*, *Nature nanotechnology* **6**, 815 (Dec, 2011).
37. J. Szejtli, *Chem Rev* **98**, 1743 (Jul 30, 1998).
38. F. Wang, E. Blanco, H. Ai, D. A. Boothman, J. Gao, *J Pharm Sci* **95**, 2309 (Oct, 2006).
39. H. Hamada, K. Ishihara, N. Masuoka, K. Mikuni, N. Nakajima, *J Biosci Bioeng* **102**, 369 (Oct, 2006).
40. C. M. Yam, Z. Xiao, J. Gu, S. Boutet, C. Cai, *J Am Chem Soc* **125**, 7498 (Jun 25, 2003).
41. R. Zhu *et al.*, *Nature nanotechnology* **5**, 788 (Nov, 2010).
42. S. M. Moghimi, A. C. Hunter, J. C. Murray, *Pharmacol Rev* **53**, 283 (Jun, 2001).
43. Q. H. Sun, M. Radosz, Y. Q. Shen, *Journal of Controlled Release* **164**, 156 (Dec 10, 2012).
44. M. Kojic, N. Filipovic, B. Stojanovic, N. Kojic, *Computer modeling in bioengineering: Theoretical background, examples and software*. J Wiley and Sons (2008), vol. 195, pp. 121-146.

45. A. Ziemys *et al.*, *Journal of Computational Physics* **230**, 5722 (2011).
46. M. Kojic, M. Milosevic, N. Kojic, M. Ferrari, A. Ziemys, *Journal of the Serbian Society for Computational Mechanics/Vol* **5**, 104 (2011).
47. M. Kojic, R. Slavkovic, M. Zivkovic, N. Grujovic, *Faculty of Mechanical Engineering University of Kragujevac, Yugoslavia*, (1996).
48. H. E. Pence, A. Williams, *Journal of Chemical Education* **87**, 1123 (2010).
49. P.-O. Gendron, F. Avaltroni, K. Wilkinson, *Journal of Fluorescence* **18**, 1093 (2008).
50. K. Palo *et al.*, *Biophysical Journal* **83**, 605 (2002).
51. J. Araujo *et al.*, *Colloids Surf B Biointerfaces* **72**, 48 (Aug 1, 2009).
52. S. Yandrapu, U. B. Kompella, *J Ocul Pharmacol Ther* **29**, 236 (Mar, 2013).
53. S. Ferrati *et al.*, *Nanoscale* **2**, 1512 (Aug, 2010).
54. R. Qi *et al.*, *Journal of controlled release : official journal of the Controlled Release Society* **159**, 251 (Apr 30, 2012).
55. L. S. Faried *et al.*, *Eur J Cancer* **42**, 934 (May, 2006).
56. T. Haritunians *et al.*, *Leukemia* **21**, 333 (Feb, 2007).
57. M. Campone *et al.*, *Br J Cancer* **100**, 315 (Jan 27, 2009).
58. C. Sessa *et al.*, *Annals of oncology : official journal of the European Society for Medical Oncology / ESMO* **21**, 1315 (Jun, 2010).
59. J. Dong *et al.*, *Cancer research* **65**, 1961 (Mar 1, 2005).
60. D. J. VanderWeele, R. Zhou, C. M. Rudin, *Molecular cancer therapeutics* **3**, 1605 (Dec, 2004).
61. S. Y. Sun *et al.*, *Cancer research* **65**, 7052 (Aug 15, 2005).
62. F. Meric-Bernstam *et al.*, *Clin Cancer Res* **18**, 1777 (Mar 15, 2012).
63. K. E. O'Reilly *et al.*, *Cancer research* **66**, 1500 (Feb 1, 2006).
64. A. Sunters *et al.*, *Cancer research* **66**, 212 (Jan 1, 2006).

Appendix

N/A